

Numerical simulations of an ocean/continent convergent system: influence of subduction geometry and mantle wedge hydration on crustal recycling.

M. Roda

Sezione di Geofisica, Dipartimento di Scienze della Terra Ardito Desio,
Università degli Studi di Milano, Italia.

A. M. Marotta

Sezione di Geofisica, Dipartimento di Scienze della Terra Ardito Desio,
Università degli Studi di Milano, Italia.

M. I. Spalla

Sezione di Geologia, Dipartimento di Scienze della Terra Ardito Desio,
Università degli Studi di Milano, Italia.

M. Roda, Università degli Studi di Milano, Dipartimento di Scienze della Terra A. Desio,
Sezione di Geofisica, Via L. Cicognara 7, 20129 Milano, Italy. (manuel.roda@unimi.it).

A. M. Marotta, Università degli Studi di Milano, Dipartimento di Scienze della Terra A. Desio,
Sezione di Geofisica, Via L. Cicognara 7, 20129 Milano, Italy. Università degli Studi di Milano,
Italy. (anna.maria.marotta@unimi.it).

M. I. Spalla, Università degli Studi di Milano, Dipartimento di Scienze della Terra A.
Desio Sezione di Geologia, and C.N.R.-I.D.P.A., Via Mangiagalli, 34, 20133, Milano, Italy.

Abstract.

The effects of the hydration mechanism on continental crust recycling are analyzed through a 2D finite element thermo-mechanical model. Oceanic slab dehydration and consequent mantle wedge hydration are implemented using a dynamic method. Hydration is accomplished by lawsonite and serpentine breakdown; topography is treated as a free surface. Subduction rates of 1, 3, 5, 7.5 and 10 cm/y, slab angles of 30°, 45° and 60° and a mantle rheology represented by dry dunite and dry olivine flow laws, have been taken into account during successive numerical experiments. Model predictions pointed out that a direct relationship exists between mantle rheology and the amount of recycled crustal material: the larger the viscosity contrast between hydrated and dry mantle, the larger the percentage of recycled material into the mantle wedge. Slab dip variation has a moderate impact on the recycling. Metamorphic evolution of recycled material is influenced by subduction style. T_{Pmax} , generally representative of eclogite facies conditions, is sensitive to changes in slab dip. A direct relationship between subduction rate and exhumation rate results for different slab dips that does not depend on the used mantle flow law. Thermal regimes predicted by different numerical models are compared to PT paths followed by continental crustal slices involved in ancient and recent subduction zones, making ablative subduction a suitable pre-collisional mechanism for burial and exhumation of continental crust.

(iole.spalla@unimi.it).

1. Introduction

In ocean-continent subduction, crustal material dragged into the subduction zone is composed mainly of ocean crust and sediments, trench sediments and continental slices belonging to the subducting plate (microcontinent) [Ring and Layer, 2003] or early continental collision [Chemenda *et al.*, 1995] or continental slices tectonically eroded from the overriding plate (ablative subduction) [Polino *et al.*, 1990; Tao and O'Connell, 1992; Spalla *et al.*, 1996]. To explain the mechanism causing the exhumation of subducted HP and UHP crustal material (either continental and/or oceanic), several models have been developed during the last 20 years. These models can be grouped into six main classes: a) crust-mantle delamination [Chemenda *et al.*, 1995], in which crustal rocks exhumation is caused by a continuous underthrusting of eroded portions of the subducting plate; b) slab break-off [Ernst *et al.*, 1997], in which the exhumation of crustal slices is consequent to the rebound induced slab-breakoff; c) slab retreat [Ring and Layer, 2003], in which the continuous underthrusting of continental slices, belonging to the subducting plate, drives the extrusion of HP continental fragments and the retreat of the slab; d) roll-back slab [Brun and Faccenna, 2008], in which buoyancy forces combined to trench retreat due to the roll-back of the slab, triggered by subduction rate decrease and slab dip increase after collision, drive the exhumation of HP crustal slices; e) decoupling of two main ductile layers [Yamato *et al.*, 2008], in which mainly negative buoyancy and/or faulting drive exhumation; f) subduction channel flow [Stockhert and Gerya, 2005], in which the exhumation is driven by the upwelling flow developed in a low-viscosity mantle wedge.

Although all of the cited mechanisms give an explanation for the exhumation of crustal continental rocks, only the channel flow model takes into account the recirculation of continental slices dragged at high depth by ablation, during active subduction before the continental collision. Actually, models a, b and c imply subduction of continental material belonging to the subducting plate during the collision of a microcontinent or a thinned continental margin. In these models, a radical change in the thermal regime occurs due to upwelling of the asthenospheric mantle (b, c and d; [*Cloos and Shreve, 1988a*]) and/or continental collision (a, c and d; [*Cloos, 1993; Gerya et al., 2008a*]), controlling the exhumation paths. Moreover, model e implies a large extension of the accretionary wedge (up to 50 km) composed mainly by sediments, a characteristic that is not present in the broader spectrum of subduction zones where higher thicknesses are less than 20 km [*Lallemand, 1999; Clift and Vannucchi, 2004; Guillot et al., 2009*].

Several pressure-temperature paths (PT-paths) and geochronological data suggest that continental crust slices are exhumed, often associated with serpentized peridotites, during active oceanic subduction [*Spalla et al., 1996; Zucali et al., 2002; Hattori and Guillot, 2003*]. Petrological models [e.g., *Schmidt and Poli, 1998; Ernst and Liou, 2008*], numerical simulations [e.g., *Arcay et al., 2005; Gerya and Stockhert, 2002; Stockhert and Gerya, 2005*] and seismic images [e.g., *Rondenay et al., 2008*] reveal that the dehydration process of the oceanic slab and consequent mantle wedge hydration have a primary role of developing a forced flow along the subduction zone, driven by viscosity and density contrasts. Furthermore, numerical models of subduction zones [*Gerya and Stockhert, 2005; Meda et al., 2010*] suggest that a large amount of subducted continental material can be exhumed from the subduction wedge to subsurface structural levels prior to collision. In

addition, natural PT data, from subducted continental crust, have been compared with model predictions only for a portion of the Alps, in which continental material underwent eclogitization and subsequent exhumation under very low temperature conditions [Meda *et al.*, 2010].

In order to verify if natural PT data from continental crust re-equilibrated under HP-LT conditions in other envisaged geodynamic scenario, from other orogenic belts and during different times (from about 400 Ma to about 20 Ma, peak age), can be consequent to the dynamics developed within a hydrated mantle wedge, we perform a parametric analysis using a 2D finite element thermo-mechanical model of ablative subduction with mantle wedge hydration. Another goal of this numerical experiment is to explore the effects of changes in the subduction rate, slab dip and mantle rheology on the P/T ratio characterizing the metamorphic climax, on the serpentinized mantle area and on the amount and rate of crustal exhumation. We present the results of a set of numerical simulations with varying subduction rates (1, 3, 5, 7.5 and 10 cm/y), slab angles (30°, 45° and 60°) and mantle rheology (serpentine, dry dunite and dry olivine flow laws). Finally, numerical model results are compared to PT paths obtained from ancient and recent subduction zones with different slab dips and convergence velocities to make the geodynamic model more quantitative.

2. Numerical modeling

The physics of the crust-mantle system during subduction is described by the coupled equations for continuity, conservation of momentum and conservation of energy, expressed

in the form:

$$\nabla \cdot \vec{v} = 0 \quad (1)$$

$$\frac{\partial \tau_{ij}}{\partial x_j} = \frac{\partial p}{\partial x_i} - \rho \vec{g} \quad (2)$$

$$\rho c \left(\frac{\partial T}{\partial t} + \vec{v} \cdot \nabla T \right) = -\nabla \cdot (-K \nabla T) + \rho H \quad (3)$$

respectively, where ρ is the density, \vec{v} the velocity, p the pressure, \vec{g} the gravity acceleration, τ_{ij} the deviatoric stress tensor, c the thermal capacity at constant pressure, T the temperature, K the thermal conductivity and H the heat production rate per unit mass. Equations (1), (2) and (3) are solved by means of the 2D finite element code SubMar [Marotta et al., 2006; Marotta and Spalla, 2007], here modified to account for mantle wedge hydration mechanism and erosion/sedimentation processes, as described in the next paragraph. Integration of equation (2) is performed using the penalty function formulation. Temporal integration of equation (3) is performed using the upwind Petrov-Galerkin method and with a fixed time step of 0.1 My.

2.1. Geometry and boundary conditions

The numerical solution of (1), (2) and (3) is performed in a 2-D domain 1400 km wide and 708 km deep (Figure 1), discretized by an irregular grid, composed by 2808 quadratic triangles and 6000 nodes. The linear size of the elements ranges from 2 km, in the mantle wedge area, to 20 km at the margin of the model. Some results of the resolution tests performed initially are presented in Appendix A. Materials (Table 1) are compositionally differentiated via the Lagrangian particle technique [Christensen, 1992]. At the beginning of each simulation, 973080 markers, identified by different indexes, are distributed with a density of 1 marker per 0.25 km² to define the atmosphere, the sediments, the oceanic

crust, the continental crust and the lithospheric mantle. The position of the individual particles during the evolution of the system is calculated by applying the first order (both in time and in space) Runge-Kutta scheme (Appendix B).

To study the effects of mantle rheology variations, a dry dunite and a dry olivine flow law are chosen to represent two different unserpentinized mantle rheologies. A constant viscosity of $10^{19} \text{ Pa}\cdot\text{s}$ is chosen to approximate the serpentinized mantle flow law according to *Honda and Saito* [2003], *Gerya and Stockhert* [2005] and *Meda et al.* [2010]. Velocity boundary conditions correspond to zero velocity ($v_x = 0$; $v_y = 0$) imposed along all boundaries of the 2D domain, with the exception of the uppermost 80 km of the vertical left side, along which $dv_x/dx = 0$ and $v_y = 0$ are imposed. To simulate plate convergence, we fix the velocity along the upper boundary of the oceanic plate, at 0 km depth, varying from 1 to 10 cm/y for the different simulations. In order to force the starting of subduction, we fix the same velocity up to 80 km depth, at the nodes of the numerical grid distributed along a dip ranging from 30° to 45° and 60° .

Thermal boundary conditions correspond to fixed temperatures at the 8 km thick uppermost atmospheric layer (from 8 to 0 km depth) and at the bottom of the model domain, 300 K and 1600 K, respectively, and to zero thermal flux through the vertical sidewalls. The initial thermal configuration corresponds to a constant temperature of 300 K in the atmosphere, a uniform upper purely conductive thermal boundary layer throughout the lithosphere (from 0 to 80 km depth and from 300 K to 1600 K) and a uniform sub-lithospheric temperature of 1600 K. The isotherm 1600 K represents the base of the lithosphere throughout the evolution of the system.

The assumed model features cause a strong coupling (i.e. high friction) between the upper and lower plates, making our models representative of the sole erosive margin type, which represent about the 60% of the global active margins [*Clift and Vannucchi, 2004*].

2.2. Topographic surface

The topographic surface is treated as a free surface between the crust and the low density, low viscosity layer that simulates the atmosphere (8 km thick). Erosion and sedimentation processes are simulated by evaluating, at each time step, the size of the accretionary prism, which is generated by the combined effects of oceanic plate bending and the ablation of the overriding plate. We simulated the instantaneous erosion of continental crust and the consequent (total or partial) filling of the accretionary prism by using a substitution technique, in which all the crustal particles lying above 2 km are replaced with air particles, and an equal number of sediment particles are introduced into the trench region (to respect global mass conservation), This procedure reproduces the erosion and sedimentation rates variable in time, as function of the system dynamics.

2.3. Hydration and serpentinization of mantle wedge

Phase diagrams for H_2O -saturated average mantle peridotite show that in the serpentine stability field, hydrous phases have the maximum H_2O contents. The water loss related to the serpentine destabilization is greater than 50 wt%, and the water content approaches zero consequent to chlorite destabilization [*Schmidt and Poli, 1998*]. In this study the progressive mantle hydration is controlled by serpentine stability field calculated from *Schmidt and Poli* [1998] using the following equations:

$$y_{hydr} = -0.0008 \cdot T_{elem}^2 + 1.1873 \cdot T_{elem} - 418.22 \quad (4)$$

above 72.5 km depth and

$$y_{hydr} = 0.0016 \cdot T_{elem}^2 - 1.19828 \cdot T_{elem} + 320.76 \quad (5)$$

below 72.5 km depth, where y_{hydr} is the maximum hydration depth and T_{elem} is the average temperature predicted in each element. Outside of the serpentine stability field a newtonian un-serpentinized mantle behavior is assumed, represented by the dry viscosity laws of olivine or dunite.

The upper limit of hydration is fixed at 30 km depth, according to *Schmidt and Poli* [1998] who show that the most important contribution of dehydration occurs below 30 km depth. They indicate a significant water budget available until a depth of about 150–200 km. Nevertheless some subducted continental rocks, returned to the surface during continental collision, show evidence of coesite-bearing assemblages [e.g., *Groppo et al.*, 2009] and stishovite [*Liu et al.*, 2008] that induce to consider the transport of water efficient until greater depths (up to 250–300 km). For this reason, we simulate the maximum dehydration depth of the oceanic crust using the following lawsonite stability field:

$$y_{dehy} = -\frac{T_{elem} + 0.8755}{714.55} \quad (6)$$

where y_{dehy} is the maximum dehydration depth, below which the water content in hydrous phases in H_2O -saturated MORB basalt is negligible [*Schmidt and Poli*, 1998]. We applied this equation until a 300 km depth. The equations cited above define the hydration field, in which we assume that material exhibits a constant viscosity of $10^{19} Pa \cdot s$ [*Arcay et al.*, 2005; *Gerya and Stockhert*, 2005] and the mantle density decrease to $3000 kg/m^3$ [*Schmidt and Poli*, 1998; *Juteau and Maury*, 1999]. Since less than 20% of the oceanic floor has been

estimated to be affected by fracture zones with serpentinization (at depth less than 5-7 km) and thus, the amount of serpentinized peridotite within the subducting lithosphere is less than 10% [Juteau and Maury, 1999] we do not introduce a further serpentinized level, although some authors suggest that the subducting lithosphere could be serpentinized [e.g., Yamato *et al.*, 2007].

3. Model predictions

In this section we analyze the effects of dip, subduction rate and mantle rheology changes on the thermal and dynamic evolution of the system (Table 2). We consider to be exhumed continental crust all particles that have been buried below and recycled above 40 km depth, which is the starting crustal thickness. Thus, for all simulations, we count the recycled markers to obtain the ratios of buried/exhumed material (exhumation %), the hydration area width, the average of the maximum and minimum pressure values reached by particles during burial and exhumation stages (P_{max} , P_{min}), the temperature values predicted for P_{max} ($T_{P_{max}}$) and the maximum temperature values reached by the recycled particles during the complete burial/exhumation loops (T_{max}). We also considered two exhumation rates: the maximum exhumation rate (Max. exh. rate), which is calculated from the upward velocity vectors recorded along the mantle wedge, and the total exhumation rate (Total exh. rate), which is obtained from analysis of the P-Tt-paths using the ratio between ($Y_{P_{max}} - Y_{P_{min}}$) and the time span.

3.1. 30° dip simulations

For the dry dunite runs, ablative subduction starts in the early stages and affects both upper and lower continental markers (See an example in Figure 2). This dynamics

dominate until the serpentinized mantle wedge area exceeds a critical size (from 1800 to 3250 km^2 , Figure 3) sufficient to develop a counter-clockwise flow into the mantle wedge, which drives the exhumation process (Figure 2b). During the mature stages of subduction, the exhumation of continental markers becomes the most important process within the mantle wedge. The combined effect of ablation and upwelling flow induces the thermal and mechanical erosion of the overriding plate along a zone extending from 100 to about 200 km from the trench. Consequent lower crust denudation occurs with a contemporaneous accretion of the exhumed crustal material, trench sediments and crustal and lithospheric mantle rocks into the subduction zone, from the surface to about 50-80 km depth (Figure 2c and f). In the serpentinized mantle wedge, a continuous counter-clockwise flow allows the recycled crustal markers to reach shallow levels (Figure 2c). Only part of the recycled material is exhumed near the surface: several particles can remain in a deep portion of the mantle wedge or can be totally buried (Figure 2c). Generally, two main vortical flows develop: one near the surface and one within the mantle wedge (Figure 2c and f).

The increase of subduction velocities induces a decrease in the dip of the oceanic slab (Figure 4b). Velocity also influences the mantle wedge kinematics: for slow subduction (1 cm/y) the less efficient counter-clockwise flow is not sufficient to allow the exhumation of a discrete crustal mass. On the contrary, the accretionary prism is well developed, and a large sediment mass is buried. The fastest subduction zones simulated (10 cm/y) show a well-developed counter-clockwise flow, and a large amount of recycled markers is carried up to the surface (Figure 4b). The accretionary prism is not well-developed, and a small mass of sediments is buried to depth. At medium subduction rates (3-5 cm/y), the exhumation percentage is the highest; this is due to the dominance of the upwelling

flow on the burial flow. In contrast, for fast subduction, burial flow dominates over the upwelling flow, preventing a large exhumation percentage.

The thermal patterns are also strongly affected by the subduction velocity, with a moderate increase of thermal erosion for fast subduction. In general, however, we observe a prevalence of conduction rather than advection in all models, due to the low angle of the subducting plate and consequent low thermal erosion for all subductions. The hydration area is also affected by the subduction plate velocity, reaching a maximum value for medium subduction rates (3 and 5 cm/y; Figure 3a, blue dots).

A statistical analysis of recycled crustal particles reveals that the markers reach a maximum mean pressure of 1.4-1.65 GPa (1.85 GPa maximum peak pressure) before exhumation, with a moderate dependence on the subduction rate. T_{Pmax} values (Figure 5a) range between 350°C and 700°C and are similar to T_{max} values recorded by the markers during burial/exhumation loops. This result reflects the low thermal gradients prediction along the mantle wedge and is due to the low subduction angle. The exhumation rate generally increases linearly with the subduction rate. Maximum exhumation rates are about 1/3 of subduction velocity (Figure 5c). Total exhumation rates are one order of magnitude lower than the maximum exhumation rate. This difference is due to the non-linear trajectories of particles during the upwelling. Although the exhumation rate increases with the subduction rate, low exhumation percentages are recorded for both slow and fast subductions. The general trend of exhumation percentage, as a function of the subduction rate, is quite similar to that of the hydration area: this suggests a direct correlation between the hydration area and the amount of exhumed material.

Upon increasing mantle viscosity, achieved by switching from a dry dunite rheology to dry olivine (Table 1), a decrease of the slab dip is observed. The thermal and kinematic structure is also influenced, with consequent variations in hydration area. In fact, the hydration area displays a moderate increase for high subduction rates, with an opposite behavior with respect to dry dunite runs (Figure 3a, green lines). Under a change in rheology the ratio of buried/exhumed particles increases (but with the same subduction rate dependence) because of strong viscosity gradients at the transition between the hydrated and dry mantle (Figure 5e, green dots). P_{max} increases to a mean maximum value of 1.8 GPa (2.25 GPa maximum peak pressure) along with increases in T_{max} and T_{Pmax} (Figure 5f, b and a, green dots). Same as hydration area also exhumation percentage displays an increase for fast subduction (7.5-10 cm/y) (Figure 5e, green dots).

3.2. 45° dip simulations

Same as in the 30° dry dunite runs, ablative subduction dominates during the early subduction stages whilst, in the late stages, lithospheric mantle denudation together with lower crust occurs (Figure 4c and d). In contrast to the previous model, slab velocity seems not to affect variations of the dip of the oceanic plate with depth. Thermal and mechanical erosion of the overriding plate is weak for slower subductions, and the accretionary prism is well-developed but lesser than in 30° simulations. The fastest subduction (10 cm/y) simulations show a dominant advective mantle flow, which allows significant thermal and mechanical erosion on the overriding plate, out to 300 km from the trench, with lower crust and lithospheric mantle denudation (Figure 4d). In slow subduction, thermal gradients along mantle wedge are low, and the counter-clockwise flow is weak (Figure 4c). In

contrast, in fast subduction zones, thermal gradients along the mantle wedge are very high, and isotherms are very close to the slab surface.

The hydration area linearly decreases with increasing subduction rate (Figure 3b, blue lines). In contrast to the 30° simulation only one counter-clockwise flow cell develops in the mantle wedge for the different subduction rates. It is worth stressing that the hydration areas predicted by 45° model (Figure 5b) are one order of magnitude lower than those predicted by 30° simulation.

Analysis of recycled crustal particles yields a mean P_{max} of 1.45-1.65 GPa with a maximum values for subduction rate of 5 cm/y. A peak pressure of 1.9 GPa is reached for the 5 cm/y model (Figure 6f, blue full dots). The $T_{P_{max}}$ values range between 400°C and 650°C and are lower than the T_{max} recorded by the markers during burial/exhumation loops, especially for medium and fast subduction rates (Figure 6a and b, blue full dots). Moreover, $T_{P_{max}}$ and T_{max} values are higher than those predicted by the 30° runs. This result suggests that the increase of advective mantle flow is related to the increase in subduction rate and dip, generating a strong thermal gradient in the upper part of the mantle wedge. Like P_{max} , the exhumation percentages are also affected by subduction velocity and the maximum values of exhumation are recorded for medium/fast subduction rates (3-5-7.5 cm/y, Figure 6e, blue full dots). Although a high exhumation area is recorded for very slow subduction (1 cm/y; Figure 3b), a small amount of exhumed material is predicted (Figure 6e, blue dots). As already pointed out for 30° simulations, this result can be due to the lower efficacy of upwelling flow with respect to the burial flow. As seen for the 30° dip cases, the change in mantle rheology from dry dunite to dry olivine increases the smoothing of the slab angle during subduction and we observe more exhumed crustal

material and higher mean P_{max} values, which reach 1.8-2.0 GPa for medium velocities. The maximum P_{max} value reaches about 2.35 GPa for the 3 cm/y model (Figure 6e and f, green full dots).

3.3. 60° dip simulations

For dry dunite runs, slab geometry displays an increase of slab dip at about 150-200 km depth, until it reaches a near vertical dip (Figure 4e and f). In contrast to the 30° and 45° cases, ablative subduction of upper and lower continental crust is less important, due to the smaller coupling between ocean and continent. Counter-clockwise flow is weak and localized in a narrow area from 60 km to 100 km depth (Figure 4f). Thermal erosion is strong for medium and fast subduction until 200 km from the trench. The accretionary prism is already less developed and is absent in fast subduction zones (Figure 3e and f). Advective mantle flow is quite important from the early stages of subduction and thermal and mechanical erosion dominate over all stages with a rapid denudation of the lower continental crust and lithospheric mantle of the overriding plate, until 250 km from the trench (Figure 3c). As a consequence, only a small percentage of subducted particles is exhumed to the surface (Figure 7e).

As in the previous simulations, a no-hydrated (white) area, is located in the mantle wedge, entrapped among the upper plate, the ablated continental crust and the hydrated mantle. Part of it is attributable to the P-T conditions de facto out of the chosen serpentine stability field. In the remnant part, although the predicted local P-T conditions might be favorable to mantle hydration, hydration actually does not occur since we have fixed the upper limit of hydration at 30 km depth, in agreement with *Schmidt and Poli*

[1998], who showed that the most important contribution of dehydration occurs below 30 km depth, as already specified in the numerical modeling section.

High dip models show a relative high exhumed/buried particles ratio for slow subduction models (1-3 cm/y) and the ratio decreases with velocity increase (Figure 7e, blue full dots). Furthermore, only for slow subduction, a discrete lithospheric mantle-crust mixing occurs into the mantle wedge (Figure 4e). Analysis on recycled crustal particles show a low P_{max} values (max 1.8 GPa) and a similar range of T_{max} and $T_{P_{max}}$ (from 600°C to 800°C), both higher than those in the 30° simulations, according to the high increase of advective flow (Figure 7f, b and a, respectively). An increase of the mantle viscosity, from dry dunite to dry olivine, induces a general decrease of hydration area for low and medium velocities (Figure 5c).

4. Natural cases

Twelve case histories from seven different subduction complexes, variably distributed in space and time, were chosen to compare numerical results and natural PT estimates. All natural cases referred to ocean-continent or ocean-arc subduction zones and we sorted PT data obtained for exhumed continental rocks regardless the interpreted provenance of the subducted continental material. This has been done to verify if the natural paleo-geothermal environments are consistent with those simulated during our numerical experiments, to check if ablative subduction represents a good alternative mechanism with respect to the different geodynamic interpretations proposed for each case. Slab angles and velocities of ancient subduction zones were obtained from more recent and widely accepted interpretations, except for the Paleozoic subductions (Urals and Armorica), which

are compared with all simulations due to the lack of suggestions about the subduction dip and rates (Table 3).

For the Alpine subduction, PT estimates from units belonging to the Western (Sesia-Lanzo Zone), Central (Languard-Campo Unit) and Eastern (Koralpe-Saualpe Unit) Austroalpine domain have been selected. Lithologic affinities between the protholiths of Austroalpine and Southalpine rocks (Adria Alpine hinterland) suggest that the provenance of this domain was from the overriding continental plate of the Alpine subduction [e.g., *Compagnoni*, 1977]. Geochronological data show that the eclogitic imprint in the internal complexes of the Western Austroalpine is Late Cretaceous (65 ± 5 Ma) ([*Meda et al.*, 2010], and refs. therein), while in the external complexes is of Eocene age (49-40 Ma) [*Dal Piaz et al.*, 2001]. Dating on eclogitic peak of the meta-ophiolitic units in Western Alps (Zermatt-Saas) show similar ages (50-38 Ma) [*Lapen et al.*, 2003]. These results and the PT evolutions inferred for different complexes of the Sesia-Lanzo Zone [e.g., *Pognante*, 1989, 1991; *Meda et al.*, 2010], often supported by detailed fieldwork [e.g., *Zucali*, 2002; *Zucali et al.*, 2002, 2004; *Babist et al.*, 2006], suggest that the exhumation of this Austroalpine continental crust occurred when oceanic subduction was still active. In addition, the age of greenschist retrogradation in the Austroalpine domain (45-37 Ma in Sesia-Lanzo zone) is within the time span of the eclogitic peak recorded in the meta-ophiolites of Zermatt-Saas, testifying that exhumation occurred under LP/LT conditions during active oceanic subduction [e.g., *Zanoni et al.*, 2008]. On the base of radiometric data the HP/LT metamorphism recorded in Central and Eastern Austroalpine domains is interpreted as early-Alpine (Late Cretaceous in age, e.g. Languard-Campo Unit [*Gazzola et al.*, 2000] and Koralpe-Saualpe Unit [*Thoni and Miller*, 1996]). In addition the

thermal regime characterizing the earlier Alpine deformation and the mineral ages in the Languard-Campo Unit are consistent with an early subduction, preceding the lower T/depth ratio characterizing the majority of early Alpine eclogites [*Gazzola et al.*, 2000]. For these reasons, the Austroalpine rocks, affected by HP Alpine metamorphism, have been mainly interpreted as the result of an ablative subduction process active at the margin of the overriding Adria plate during pre-collisional stages of the Alpine convergence. This is in agreement with geodynamic models at the scale of the whole belt, implying subduction and exhumation of the Austroalpine crust before continental collision [*Platt*, 1987; *Polino et al.*, 1990; *Spalla et al.*, 1996; *Stockhert and Gerya*, 2005].

For the Aegean subduction, continental rocks of the Cyclades Blueschists Unit and of the Phyllite-Quartzite Unit are taken into account. The Cyclades Blueschists Unit consists of metasediment originally belonging to the Cycladic passive margin, which was the eastern part of the Adria basement with an HP/LT metamorphic imprint (55-60 Ma in age) [*Ring and Layer*, 2003]. The Phyllite-Quartzite Unit is a Carboniferous to Middle Triassic sedimentary sequence with an HP/LT metamorphic imprint (19-24 Ma in age). This unit represents a former part of the Adria micro-continent [*Thomson et al.*, 1998]. The progressive rejuvenation of HP/LT toward South, the southern arc migration and the intermingling of both oceanic and continental exhumed slices have been justified using slab retreat [*Ring and Layer*, 2003] or rollback slab [*Brun and Faccenna*, 2008] models. These mechanisms are assumed to explain also the metamorphic evolution of the Turkey units, which have been involved in Aegean subduction.

For the Calabrian examples, HP continental metasediments and marble have been interpreted as the exhumation of HP rocks along an orogenic wedge by *Rossetti et al.* [2004],

while *Ring and Layer* [2003] suggest a rollback slab mechanism to explain the exhumation of the HP/LT Calabrian units and related back-arc extension of the southern Tyrrhenian area. For the Alaskan Brooks Range Metamorphic Belt, an arc-continent collision is proposed to justify the exhumation of HP/LT continental rocks [*Till and Snee*, 1996]. For the metapelites of the Ile de Groix belonging to the Armorica Massif, we take into account the possibility that they could derive from continental sediments [*Bernard-Griffiths et al.*, 1986]. Thrusting of HP units (Upper Unit) onto low-grade units (Lower Unit) is proposed to explain the exhumation of these rocks occurring after the HP event, implying bulk horizontal shortening [*Bosse et al.*, 2002]. *Leech and Ernst* [2000] suggest a synconvergent exhumation of the HP and UHP metasediment belonging to the East European platform, accomplished by a combination of west-directed thrusting followed by normal faulting.

The characteristics of these natural subduction zones are summarized in Table 3; rock types, slab dips, convergent velocities, P-T climax, exhumation rates and relative references are reported. To infer the slab dip of the ancient Calabrian and Alpine subduction zones, the west-east upper mantle flow criterion [*Doglioni et al.*, 2007] is used. As was already pointed out, Paleozoic subductions have been compared with the predictions obtained from all the simulations.

Simulated PT climax assemblages of slow subduction rates and low to moderate subduction angles (Aegean, Alps and Turkey) are in good agreement with numerical predictions, especially for a 3 cm/y slab velocity. Temperatures, in turn, are in the simulation range, regardless of the subduction rate. Very HP cases, like the Aegean Cyclades Blueschists and Alps1, are in agreement with both 30° and 45° slab dip models for a velocity of 3 cm/y. Steeper dips seem to be a better configuration for the Calabrian subduction. The

metamorphic evolution of the Alaskan and the Paleozoic subduction zones show a good agreement with PT predictions of moderate to fast subduction simulations, without a particular dip constraint (Figure 8).

As a function of subduction velocity, natural exhumation rates are comparable to the simulated exhumation rates, as obtained from PTt-paths (total exhumation rates, Figure 9). Only Aegean1 shows an exhumation rate higher than those predicted, although it is of the same order of magnitude. The maximum exhumation rates, which are obtained from the modulus of the upwelling flow vectors, are one order of magnitude higher than those obtained from PTt-paths, and they are not compatible with the natural exhumation rates (Figure 9). This discrepancy could be due to the non-linear trajectories of crustal particles during the exhumation stages.

We find generally good agreement between natural PT evolution and numerical predictions. In addition, the Paleozoic systems are characterized by PT estimates compatible with predictions from fast subduction zones (>5 cm/y). Natural exhumation rates are comparable to the predicted ones, if obtained from the analysis of simulated PTt-paths. Moreover, exhumation rates are one order of magnitude lower than the subduction rates. This finding is in contrast with some natural examples of UHP, like Dora-Maira, in the Western Alps [Rubatto and Hermann, 2001], Papua New Guinea [Baldwin *et al.*, 2004] and Tinos, in the Aegean [Brun and Faccenna, 2008], which all show exhumation rates equal to or higher than the subduction rates. Also, some numerical models [Gerya *et al.*, 2008a; Warren *et al.*, 2008] display high exhumation rates. Nevertheless, the evolution of both Dora-Maira and Papua New Guinea and the cited simulations refer to collisions, when the amount of crustal mass buried at depth might generate a transient channel into

the mantle wedge with high temperature and strong positive buoyancy, allowing for fast exhumation of the crustal material [Gerya *et al.*, 2008a]. Alternatively, Brun and Faccenna [2008] indicate that high exhumation rates (of up to 30 mm/y) characterize the first stage of the exhumation of UHP rocks. This finding is in agreement with the results of the numerical model of Yamato *et al.* [2008] which shows a high exhumation rate (about 1 cm/y) only for the first stage of the exhumation path. As reported by Zucali *et al.* [2002], the exhumation rates obtained from complete PTt-paths of early ocean/continent subduction stages are one order of magnitude lower than subduction rates, as pointed out by the worldwide subduction review by Agard *et al.* [2009]. Thus, the higher exhumation rates may refer to either collisional events or to pre-collisional transient stages.

5. Comparison with other numerical models of subduction zones

In this section we compare our results with the results of other numerical models accounting for pre/early-collisional exhumation of crustal rocks. Specifically, we focus on subduction flow models [e.g., Stockhert and Gerya, 2005; Faccenda *et al.*, 2009] and on exhumation in accretionary wedge models [e.g., Yamato *et al.*, 2007].

Pre-collisional exhumation of HP-LT crustal rocks is treated in Gerya and Stockhert [2005] and Stockhert and Gerya [2005] using a 2D finite difference model in which mantle wedge hydration is included. Our model takes into account similar dehydration/hydration mechanisms and comparable rheological parameter for the mantle wedge material. However we implemented a different numerical approach using a finite element method with Lagrangian particles technique instead of finite differences and marker-in-cell particle technique. Furthermore we forced the subduction using fixed velocities until 80 km depth upon the oceanic crust in contrast to a fixed weak zone imposed by Gerya and Stockhert

[2005]. Moreover we have not implemented a fixed erosion/sedimentation rates but they are variable within the subduction dynamics. In order to contribute to fill the gap about the influence of subduction setting on crustal exhumation we performed a parametric analysis on variable dip, velocity and mantle rheology.

In agreement with *Stockhert and Gerya* [2005] and *Faccenda et al.* [2009] we obtained pre-collisional exhumation of continental crust belonging to the overriding plate dragged to high depth by ablative subduction and also reproduced marble-cake configuration of the accretionary and mantle wedges. In contrast, we obtained lower exhumation rates, more comparable with those obtained by natural data and in addition we evaluate the fitting between natural PT data and the model predictions on geothermal gradient. Same as shown by *Gerya and Stockhert* [2005] we found a high efficiency of ablative subduction process to drag large amount on continental material to deep levels. We simulated a strong coupled plates subduction zone in order to represent an erosive margin [*Clift and Vannucchi*, 2004] and our results suggest that the amount of ablated material is proportional to the area of the plates contact and thus to the subduction dip. Furthermore, the predicted efficiency of the ablation should be considered as a maximum end-member for the erosive margins. Moreover, *Gerya et al.* [2008b], *Faccenda et al.* [2008] and *Faccenda et al.* [2009] pointed out that the introduction of shear heating and water percolation of hydrated sediments, located into the accretionary prism, may reduce the friction between the facing plates, up to totally decoupling. Thus, ablation decreases and a one-side subduction, characterized by an accretionary margin, develops [*Clift and Vannucchi*, 2004].

Within the accretionary wedge models, *Yamato et al.* [2007, 2008] pointed out the role played by the accretionary prism on the exhumation of sediments and continental rocks.

However, both the amount and the P_{max} of the exhumed materials strongly depend on the existence of an accretionary prism larger than those at present described in natural environments [Cloos and Shreve, 1988b; Guillot et al., 2009]. In addition the accretionary prism dimension depends on slab dip, subduction rate, coupling/decoupling and sedimentation/erosion rates on the size of the accretionary prism [Faccenda et al., 2009]. Furthermore, differently from our study, no continental crust exhumation occurs before the collision.

6. Summary and conclusions

The parametric analysis performed for ocean/continent convergent systems points out that ablative subduction is a highly efficient process for dragging large masses of upper and lower continental crust, belonging to the overriding plate, to deep levels. In particular, ablative subduction is much more efficient for low slab dip due to the stronger coupling between the oceanic and continental plates. The subduction rate has also been observed to have a moderate influence on ablative subduction efficiency. In addition to slab dip, in 30° simulations, the similarity of trends in hydration area and exhumation percentage with respect to subduction rates suggests that the width of the hydration area is correlated to the amount of exhumed material. Maximum values of exhumation percentage are predicted for intermediate subduction rates except in the 60° simulations, where the peak values are predicted for the lowest velocities (1 cm/y).

The maximum values of P_{max} are recorded by markers of 45° subductions, and the lowest values are predicted by 60° subduction markers. Just as for the exhumation percentage values, the maximum P_{max} is also generally predicted to occur for medium subduction rate (3-5 cm/y) in low and intermediate dip simulations (30° and 45°). T_{Pmax} and T_{max}

values display a positive correlation with the subduction angle and a low variation with subduction rate. In 30° simulations thermal gradients along the mantle wedge are low and $T_{P_{max}}$ and T_{max} values are comparable within the same subduction rates. In contrast, in 60° simulations thermal gradients increase along the mantle wedge, and strong thermal and mechanical erosion occur at the base of the overriding plate. The accretionary prism is strongly affected by the subduction rate and the subduction dip: increasing both parameters decreases the width of the prism and is accompanied by an increase in trench depth. Variations in mantle rheology affect the slab geometry for low and moderate subduction dips. We also predict a strong effect on P_{max} as recorded by crustal markers. Mantle viscosity has a positive correlation with P_{max} values due to the strong viscosity gradient generated at the transition between hydrated and dry mantle.

It is worth stressing that the small scale circulation in the wedge area, allowing a huge amount of subducted crustal markers to come back at shallow depths, occurs because of the low-viscosity subduction channel induced by the mantle hydration. The crucial role played by fluids in the whole process has been already investigated in previous works [e.g., *Gerya and Stockhert, 2002; Meda et al., 2010*]; in particular, *Meda et al. [2010]* show that no exhumation is possible without mantle hydration, before continental collision.

Natural data and model predictions are in good agreement: the thermal states simulated for ablative subduction with a hydrated mantle wedge justify the natural PT estimates obtained on continental crust units involved in ocean/continent subduction systems. Similarly, the exhumation rates obtained from analysis of PTt-paths are more compatible with natural ones than those obtained from the upwelling flow vector which could justify only

a transient exhumation stage. In general, numerical simulations and natural data show exhumation rates lower than subduction rates.

The good agreement obtained between our model and models developed using different numerical and starting approaches [e.g., *Gerya and Stockhert, 2005; Stockhert and Gerya, 2005; Faccenda et al., 2008, 2009*], except for the exhumation rates, indicates the robustness of the corner-like flow mechanism on pre-collisional exhumation of the continental crust. On the basis of these results, we propose ablative subduction of the overriding continental plate with corner-like flow as a good alternative, pre-collisional mechanism for the subduction and exhumation of continental crust, in contrast to collisional processes such as slab retreat, rollback slab or microcontinent collision.

Appendix A: Resolution Tests

In this section we present the results of the resolution test performed at the beginning of our numerical analysis to verify the persisting robustness of the used numerical code, after the introduction, within the original SubMar code [*Marotta et al., 2006*], of the mantle hydration mechanism, that drives small scale wedge circulation and exhumation of subducted crustal material. We compare the results, in terms of velocity, temperature and stream line and some statistical parameters (T_{Pmax}, T_{max} , max. exh. rate, P_{max}), obtained by three different grids, with different resolution in the wedge area. Figure 10, panels a_1 , a_2 and a_3 , compares the thermo-dynamic settings obtained in the wedge area by the grid used in the present study (grid 2, panel a_2) with those obtained by a rougher grid (grid 1, panel a_1 , minimum linear size = 5 km) and a refined grid (grid 3, panel a_3 , minimum linear size = 1 km). At large scale, both the temperature and velocity fields appear unaffected by the grid size. Furthermore, focusing on the wedge area, it is possible

to enlighten a stable circulation, although much more defined when grid 2 and grid 3 are used (panel a_1 , a_2 , a_3 , black stream lines). In this case, a huger amount of crustal material is recycled. For what concerns the statistical parameters, panels b_i generally indicate a high variability of predicted values of parameters from grid 1 to grid 2, while low changes occurs when results by grid 3 are compared with those obtained by grid 2, always within the standard deviation of the model. For this reason and for the more convenient computational time, we chose grid 2 for developing our numerical analysis.

Appendix B: Compositional differentiation

The position of the individual particles during the evolution of the system is calculated by applying the first order (both in time and space) Runge-Kutta scheme to equation $d\vec{x}/dt = \vec{v}$, with \vec{x} and \vec{v} indicating the instantaneous position and velocity of each particle, the last one evaluated by interpolating the velocities at the 6 nodes delimiting the element containing the marker through the same shape functions used in the numerical approximation. At each time step, a non-dimensional function C describes the elemental composition, calculated on the basis of the number of different type particles present in the element, such that

$$C = 1 - C_o - C_c - C_s - C_a \quad (7)$$

with $C_i = M_i/M_0$, where M_i is the number of markers of type i (mantle $i=m$, continental crust $i=c$, oceanic crust $i=o$, sediments $i=s$ and atmosphere $i=a$) within the element and M_0 is the maximum number of markers (of any type) that the element can contain.

By taking into account the elemental composition, the density of each element is calculated as

$$\rho = \rho_0^m [1 - \alpha (T - T_0)] + \nabla \rho_o^m C_o + \nabla \rho_c^m C_c + \nabla \rho_s^m C_s + \nabla \rho_a^m C_a \quad (8)$$

below the initial zero topographic level, or

$$\rho = \rho_0^a + \nabla \rho_o^a C_o + \nabla \rho_c^a C_c + \nabla \rho_s^a C_s + \nabla \rho_0^m C \quad (9)$$

above the initial zero topographic level, where ρ_0^m and ρ_0^a are the reference densities of mantle and atmosphere, respectively, $\nabla \rho_i^m = (\rho_i - \rho_m)$ and $\nabla \rho_i^a = (\rho_i - \rho_a)$ represent the difference between the density of the different materials (ρ_i) and the reference density of the mantle (ρ_m) or the atmosphere (ρ_a). α is the thermal expansion coefficient. For what concerns the rheology, a viscous behavior is assumed for the whole system and the viscosity of each element is calculated as

$$\mu = \mu_m [1 - C_o - C_c - C_s - C_a] + \mu_o C_o + \mu_c C_c + \mu_s C_s + \mu_a C_a \quad (10)$$

below the initial zero topographic level, or

$$\mu = \mu_a C_a + \mu_o C_o + \mu_c C_c + \mu_s C_s + \mu^m C \quad (11)$$

above the initial zero topographic level, with

$$\mu_i = \mu_i^0 e^{\frac{E_{ai}}{n_i R} \left(\frac{1}{T} - \frac{1}{T_0} \right)} \quad (12)$$

where μ_i^0 is the reference viscosity of generic material i at the reference temperature T_0 , E_a^i the activation energy and T the temperature. Since only a viscous rheology is considered, the crust is expected to remain strong at much higher stresses than the brittle limit and we introduce a viscosity cut-off value of 10^{25} Pa·s to minimize this effect.

Acknowledgments. The constructive criticism of Faccenda M. and of an anonymous reviewer greatly improved the text. Prin 2008 "Tectonic trajectories of subducted lithosphere in the Alpine collisional orogen from structure, metamorphism and lithostratigraphy" and PUR 2008 "La ricerca geofisica: esplorazione, monitoraggio, elaborazione e modellazione" are gratefully acknowledged.

References

- Agard, P., P. Yamato, L. Jolivet, and E. Burov (2009), Exhumation of oceanic blueschists and eclogites in subduction zones: Timing and mechanisms, *Earth-Science Reviews*, *92*, 53–79, doi:10.1016/j.earscirev.2008.11.002.
- Arcay, D., E. Tric, and M. Doin (2005), Numerical simulation of subduction zones. Effect of slab dehydration on the mantle wedge dynamics., *Physics of the Earth and Planetary Interiors*, *149*, 133–153, doi:10.1016/j.pepi.2004.08.020.
- Babist, J., M. R. Handy, M. Konrad-Schmolke, and K. Hammerschmidt (2006), Precollisional, multistage exhumation of subducted continental crust: The Sesia Zone, western Alps, *Tectonics*, *25*(TC6008), doi:10.1029/2005TC001927.
- Baldwin, S. L., B. D. Monteleone, L. E. Webb, P. G. Fitzgerald, M. Grove, and E. J. Hill (2004), Pliocene eclogite exhumation at plate tectonic rates in eastern Papua New Guinea, *Nature*, *431*(263-267), doi:10.1038/nature02846.
- Ballevre, M., P. Pitra, and M. Bohn (2003), Lawsonite growth in the epidote blueschists from the Ile de Groix (Armorican Massif, France): a potential geobarometer, *Journal of Metamorphic Geology*, *21*(7), 723–735, doi:10.1046/j.1525-1314.2003.00486.x.

- Bernard-Griffiths, J., M. Carpenter, J. Peucat, and B. Jahn (1986), Geochemical and isotopic characteristics of blueschist facies rocks from the Île de Groix, Armorican Massif (northwest France), *Lithos*, *19*(3-4), 235–253, doi:10.1016/0024-4937(86)90025-3.
- Best, M. G., and E. H. Christiansen (2001), *Igneous Petrology*, Blackwell Sci., London.
- Bosse, V., M. Balleve, and O. Vidal (2002), Ductile thrusting recorded by Garnet Iso-grad from Blueschist-Facies Metapelites of the Ile de Groix, Armorican Massif, France, *Journal of Petrology*, *43*(3), 485–510, doi:10.1093/petrology/43.3.485.
- Brun, J.-P., and C. Faccenna (2008), Exhumation of high-pressure rocks driven by slab rollback, *Earth and Planetary Science Letters*, *272*, 1–7, doi:10.1016/j.epsl.2008.02.038.
- Chemenda, A. I., M. Mattauer, J. Malavieille, and A. N. Bokun (1995), A mechanism for syn-collisional rock exhumation and associated normal faulting: Results from physical modelling, *Earth and Planetary Science Letters*, *132*, 225–232.
- Chopra, P. N., and M. S. Peterson (1981), The experimental deformation of dunite, *Tectonophysics*, *78*, 453–473, doi:10.1016/0040-1951(81)90024-X.
- Christensen, U. R. (1992), An Eulerian Technique for thermo-mechanical model of lithospheric extension, *Journal of Geophysical Research*, *97*, 2015–2036, doi:10.1029/91JB02642.
- Clift, P., and P. Vannucchi (2004), Control on tectonic accretion versus erosion in subduction zones: implication for the origin and recycling of the continental crust., *Review of Geophysics*, *42*, 1–31, doi:10.1029/2003RG000127.
- Cloos, M. (1993), Lithospheric buoyancy and collisional orogenesis: Subduction of oceanic plateaus, continental margins, island arcs, spreading ridges and seamounts, *Geological Society of America Bulletin*, *105*, 715–737.

Cloos, M., and R. L. Shreve (1988a), Subduction-channel model of prism accretio, melange formation, sediment subduction, and subduction erosion at convergent plate margins: 1. background and description, *PaGeoph.*, 128(3/4).

Cloos, M., and R. L. Shreve (1988b), Subduction-channel model of prism accretio, melange formation, sediment subduction, and subduction erosion at convergent plate margins: 2. implication and discussion, *PaGeoph.*, 128(3/4).

Compagnoni, R. (1977), The Sesia-Lanzo zone: high-pressure low-temperature metamorphism in the Austroalpine continental margin., *Rendiconti della Società Italiana di Mineralogia e Petrologia*, 33, 335–374.

Dal Piaz, G., G. Cortiana, A. Del Moro, S. Martin, G. Pennacchioni, and P. Tartarotti (2001), Tertiary age and paleostructural inferences of the eclogitic imprint in the Austroalpine outliers and Zermatt±Saas ophiolite, Western Alps, *Int J Earth Sci (Geol Rundsch)*, 90, 668–684, doi:10.1007/s005310000177.

Doglioni, C., E. Carminati, M. Cuffaro, and D. Scrocca (2007), Subduction kinematics and dynamic constraints, *Earth-Science Reviews*, 83, 125–175, doi:10.1016/j.earscirev.2007.04.001.

Dubois, J., and M. Diament (1997), *Géophysique*, Masson, Paris.

Ernst, W., and J. Liou (2008), High- and ultrahigh-pressure metamorphism: Past results and future prospects, *American Mineralogist*, 93, 1771–1786, doi:10.2138/am.2008.2940.

Ernst, W. G., S. Maruyama, and S. Wallis (1997), Buoyancy-driven, rapid exhumation of ultrahigh-pressure metamorphosed continental crust, *Proc. Natl. Acad. Sci.*, 94(9532-9537).

- Faccenda, M., T. V. Gerya, and S. Chakraborty (2008), Styles of post-subduction collisional orogeny: Influence of convergence velocity, crustal rheology and radiogenic heat production, *Lithos*, *103*, 257–287, doi:10.1016/j.lithos.2007.09.009.
- Faccenda, M., G. Minelli, and T. Gerya (2009), Coupled and decoupled regimes of continental collision: Numerical modeling, *Earth and Planetary Science Letters*, *278*, 337–349, doi:10.1016/j.epsl.2008.12.021.
- Gazzola, D., G. Gosso, E. Pulcrano, and M. I. Spalla (2000), Eo-Alpine HP metamorphism in the Permian intrusives from the steep belt of the central Alps (Languard-Campagna nappe and Tonale Series), *Geodinamica Acta*, *13*, 149–167.
- Gerya, T., L. Perchuk, and J. P. Burg (2008a), Transient hot channels: Perpetrating and regurgitating ultrahigh-pressure, high-temperature crust–mantle associations in collision belts, *Lithos*, *103*, 236–256, doi:10.1016/j.lithos.2007.09.017.
- Gerya, T. V., and B. Stockhert (2002), Exhumation rates of high pressure metamorphic rocks in subduction channels: The effect of rheology., *Geophysical Research Letters*, *29*(8), doi:doi:10.1029/2002TC001406.
- Gerya, T. V., and B. Stockhert (2005), Two-dimensional numerical modeling of tectonic and metamorphic histories at active continental margins, *Int J Earth Sci (Geol Rundsch)*, *95*(2), doi:10.1007/s00531-005-0035-9.
- Gerya, T. V., J. A. Connolly, and D. A. Yuen (2008b), Why is terrestrial subduction one-sided?, *Geology*, *36*(1), 43–46, doi:10.1130/G24060A.1.
- Gosso, G., B. Messiga, G. Rebay, and M. I. Spalla (2010), The interplay between deformation and metamorphism during eclogitization of amphibolites in the Sesia-Lanzo zone of the Western Alps., *International Geology Review*, *51*(12), 27, doi:

10.1080/00206810903529646.

Groppo, C., M. Beltrando, and R. Compagnoni (2009), The PT path of the ultra-high pressure Lago Di Cignana and adjoining high-pressure meta-ophiolitic units: insights into the evolution of the subducting Tethyan slab, *Journal of Metamorphic Geology*, *27*(3), 207–231, doi:10.1111/j.1525-1314.2009.00814.x.

Guillot, S., K. Hattori, P. Agard, S. Schwartz, and O. Vidal (2009), Exhumation Processes in Oceanic and Continental Subduction Contexts: A Review, in *Subduction Zone Dynamics*, edited by S. Lallemand and F. Funiciello, pp. 175–204, Springer-Verlag Berlin Heidelberg, doi:10.1007/978-3-540-87974-9.

Haenel, R., L. Rybach, and L. Stegena (1988), *Handbook of Terrestrial Heat-Flow Density Determination*, Kluwer Academic Publishers.

Hattori, K. H., and S. Guillot (2003), Volcanic fronts form as a consequence of serpentinite dehydration in the forearc mantle wedge, *Geology*, *31*(6), 525–528, doi:10.1130/0091-7613(2003)031<0525:VFFAAC>2.0.CO;2.

Honda, S., and M. Saito (2003), Small-scale convection under the back-arc occurring in the low viscosity wedge, *Earth and Planetary Science Letters*, *216*, 703–715, doi:10.1016/S0012-821X(03)00537-5.

Juteau, T., and R. Maury (1999), *The Oceanic Crust, from Accretion to Mantle Recycling*, Praxis Springer.

Karato, S., and P. Wu (1987), Rheology of the Upper Mantle: A Synthesis, *Science*, *260*(5109), 771–778, doi:10.1126/science.260.5109.771.

Kirby, S. H. (1983), Rheology of the Lithosphere, *Review of Geophysics*, *21*(6), 1459–1487, doi:10.1029/RG021i006p01458.

- Lallemand, S. (1999), *La subduction océanique*, Gordon and Breach Science Publishers.
- Lapen, T. J., C. M. Johnson, L. P. Baumgartner, N. J. Mahlen, B. L. Beard, and J. M. Amato (2003), Burial rates during prograde metamorphism of an ultra-high-pressure terrane: an example from Lago di Cignana, western Alps, Italy, *Earth and Planetary Science Letters*, *215*, 57–72, doi:10.1016/S0012-821X(03)00455-2.
- Leech, M. L., and W. Ernst (2000), Petrotectonic evolution of the high- to ultrahigh-pressure Maksyutov Complex, Karayanova area, south Ural Mountains: structural and oxygen isotope constraints, *Lithos*, *52*, 235–252, doi:10.1016/S0024-4937(99)00093-6.
- Liu, L., J. Zhang, H. W. Green, Z. Jin, and K. N. Bozhilov (2008), Evidence of former stishovite in metamorphosed sediments, implying subduction to > 350 km, *Earth and Planetary Science Letters*, *263*, 180–191, doi:10.1016/j.epsl.2007.08.010.
- Marotta, A. M., and I. Spalla (2007), Permian-Triassic high thermal regime in the Alps: Result of late Variscan collapse or continental rifting? validation by numerical modeling, *Tectonics*, *26*, doi:10.1029/2006TC002047.
- Marotta, A. M., E. Spelta, and C. Rizzetto (2006), Gravity signature of crustal subduction inferred from numerical modelling, *Geophys. J. Int.*, *166*, 923–938, doi:10.1111/j.1365-246X.2006.03058.x.
- Meda, M., A. Marotta, and M. Spalla (2010), The role of mantle hydration into the continental crust recycling in the wedge region.
- Patrick, B. (1995), High-pressure-low-temperature metamorphism of granitic orthogneiss in the Brooks Range, northern Alaska, *Journal of Metamorphic Geology*, *13*(1), 111–124, doi:10.1111/j.1525-1314.1995.tb00208.x.

Platt, J. P. (1987), The uplift high-pressure-low-temperature metamorphic rocks, in *Tectonic settings of regional metamorphism; proceedings of a Royal Society discussion meeting*, edited by E. R. Oxburgh, B. W. D. Yardley, and P. C. England, pp. 87–103, R. Soc. London, U.K.

Pognante, U. (1989), Tectonic implications of lawsonite formation in the Sesia zone (Western Alps), *Tectonophysics*, *162*, 219–227.

Pognante, U. (1991), Petrological constraints on the eclogite- and blueschist-facies metamorphism and P-T-t paths in the Western Alps., *Journal of Metamorphic Geology*, *9*, 5–17.

Polino, R., G. Dal Piaz, and G. Gosso (1990), Tectonic erosion at the Adria margin and accretionary processes for the Cretaceous orogeny of the Alps., *Mémoires de la Société Géologique de France*, *156*, 345–367.

Ranalli, G., and D. C. Murphy (1987), Rheological stratification of the lithosphere, *Tectonophysics*, *132*(4), 281–295, doi:10.1016/0040-1951(87)90348-9.

Ring, U., and P. W. Layer (2003), High-pressure metamorphism in the Aegean, eastern Mediterranean: Underplating and exhumation from the Late Cretaceous until the Miocene to Recent above the retreating Hellenic subduction zone, *Tectonics*, *22*(3), doi:10.1029/2001TC001350.

Rondenay, S., G. A. Abers, and P. E. V. Keken (2008), Seismic imaging of subduction zone metamorphism, *Geology*, *36*(4), 275–278, doi:10.1130/G24112A.1.

Rossetti, F., B. Goffé, P. Monié, C. Faccenna, and G. Vignaroli (2004), Alpine orogenic P-T-t-deformation history of the Catena Costiera area and surrounding regions (Calabrian Arc, southern Italy): The nappe edifice of north Calabria revised with insights on the

Tyrrhenian-Apennine system formation, *Tectonics*, *23*, doi:10.1029/2003TC001560.

Rubatto, D., and J. Hermann (2001), Exhumation as fast as subduction?, *Geology*, *29*, 3–6, doi:10.1130/0091-7613(2001)029<0003:EAFAS>2.0.CO;2.

Schmidt, M., and S. Poli (1998), Experimentally based water budgets for dehydrating slabs and consequences for arc magma generation, *Earth and Planetary Science Letters*, *163*, 361–379, doi:10.1016/S0012-821X(98)00142-3.

Spalla, M., J. Lardeaux, G. Dal Piaz, G. Gosso, and B. Messiga (1996), Tectonic significance of Alpine eclogites, *Journal of Geodynamics*, *21*(3), 257–285.

Stockhert, B., and T. V. Gerya (2005), Pre-collisional high pressure metamorphism and nappe tectonics at active continental margins: a numerical simulation, *Terra Nova*, *17*, 102–110, doi:10.1111/j.1365-3121.2004.00589.x.

Tao, W. C., and R. J. O’Connell (1992), Ablative subduction: A two-sided alternative to the conventional subduction model, *Journal of Geophysical Research*, *97*(B6), 8877–8904.

Thomson, S. N., B. Stöckhert, and M. R. Brix (1998), Thermochronology of the high-pressure metamorphic rocks of Crete, Greece: Implications for the speed of tectonic processes, *Geology*, *26*, 259–262, doi:10.1130/0091-7613(1998)026<0259:TOTHPM>2.3.CO;2.

Thoni, M., and C. Miller (1996), Garnet Sm–Nd data from the Saualpe and the Koralpe (Eastern Alps, Austria): chronological and P–T constraints on the thermal and tectonic history, *Journal of Metamorphic Geology*, *14*, 453–466.

Till, A. B., and L. W. Snee (1996), Ar/Ar evidence that formation of blueschists in continental crust was synchronous with foreland fold and thrust belt deformation,

western Brooks Range, Alaska, *Journal of Metamorphic Geology*, *13*(1), 41–60, doi:10.1111/j.1525-1314.1995.tb00204.x.

Warren, C. J., C. Beaumont, and R. A. Jamieson (2008), Deep subduction and rapid exhumation: Role of crustal strength and strain weakening in continental subduction and ultrahigh-pressure rock exhumation, *Tectonics*, *27*, doi:10.1029/2008TC002292.

Whitney, D. L., C. Teyssier, S. C. Kruckenberg, V. L. Morgan, and L. J. Iredale (2008), High-pressure–low-temperature metamorphism of metasedimentary rocks, southern Menderes Massif, western Turkey, *Lithos*, *101*, 218–232, doi:10.1016/j.lithos.2007.07.001.

Yamato, P., P. Agard, E. Burov, L. L. Pourhiet, L. Jolivet, and C. Tiberi (2007), Burial and exhumation in a subduction wedge: Mutual constraints from thermomechanical modeling and natural P-T-t data (Schistes Lustrés, western Alps), *Journal of Geophysical Research*, *112*, 28, doi:10.1029/2006JB004441.

Yamato, P., E. Burov, P. Agard, L. L. Pourhiet, and L. Jolivet (2008), HP-UHP exhumation during slow continental subduction: Self-consistent thermodynamically and thermomechanically coupled model with application to the Western Alps, *Earth and Planetary Science Letters*, *271*, 63–74, doi:10.1016/j.epsl.2008.03.049.

Zanoni, D., L. Bado, M. Spalla, M. Zucali, and G. Gosso (2008), Structural analysis of the northeastern margin of the tertiary intrusive stock of Biella (Western Alps, Italy), *Boll. Soc. Geol. It. (Ital. J. Geosci.)*, *127*(1), 125–140.

Zucali, M. (2002), Foliation map of the “Eclogitic Micaschists Complex” (Monte Mucrone – Monte Mars – Mombarone, Sesia-Lanzo Zone, Italy), *Memorie Scienze Geologiche*, *54*, 86–100.

Zucali, M., I. Spalla, and G. Gosso (2002), Strain partitioning and fabric evolution as a correlation tool: the example of the Eclogitic Micaschists Complex in the Sesia-Lanzo Zone (Monte Mucrone-Monte Mars, Western Alps, Italy), *Schweiz. Mineral. Petrogr. Mitt.*, *82*, 429–454.

Zucali, M., M. Spalla, G. Gosso, S. Racchetti, and F. Zulbati (2004), Prograde LWS-KY transition during subduction of the Alpine continental crust of the Sesia- Lanzo Zone: The Ivozio Complex., *Journal of the Virtual Explorer, Electronic Edition*, *16*(4).

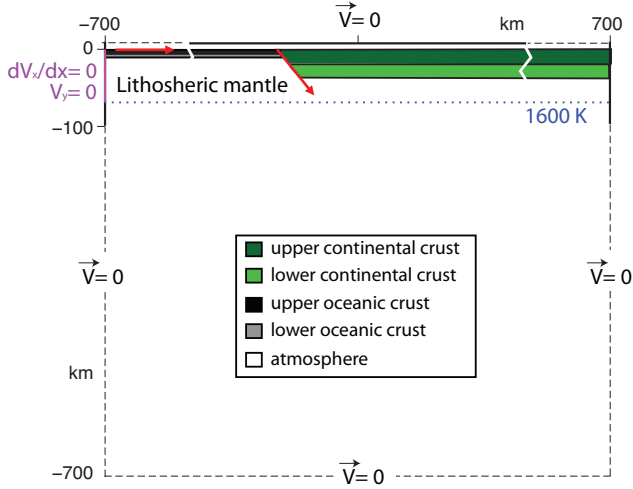


Figure 1. Model setup and boundary conditions for all of the simulations. See text for further details. The legend illustrates the marker provenance.

Table 1. Material properties. References: (a) [Ranalli and Murphy, 1987], (b) [Kirby, 1983], (c) [Chopra and Peterson, 1981], (d) [Karato and Wu, 1987], (e) [Dubois and Diament, 1997; Best and Christiansen, 2001], (f) [Haenel et al., 1988], (g) [Gerya and Stockhert, 2002].

Materials	Rheology	μ^0 ($Pa \cdot s^{-1}$)	n	ρ_0 (kg/m^3)	k (W/mK)	H_r ($\mu W/m^3$)	E (KJ/mol)	Refs.
Continental crust	Dry Granite	$3.47 \cdot 10^{21}$	3.20	2640	3.01	2.50	123	a,e,f
Oceanic crust	Diabase	$1.61 \cdot 10^{22}$	3.40	2961	2.10	0.40	260	b,e,f
Sediments	10^{19}			2640	3.01	2.50	123	e,f
Dry mantle	Dry Dunite	$5.01 \cdot 10^{20}$	3.41	3300	4.15	0.002	444	c,e,f
	Dry Olivine	$5.01 \cdot 10^{21}$	3.50	3300	4.15	0.002	540	d,e,f
Serpent. mantle	10^{19}			3000	4.15	0.002	444	e,f,g
Atmosphere	10^{23}			1.18	0.026			

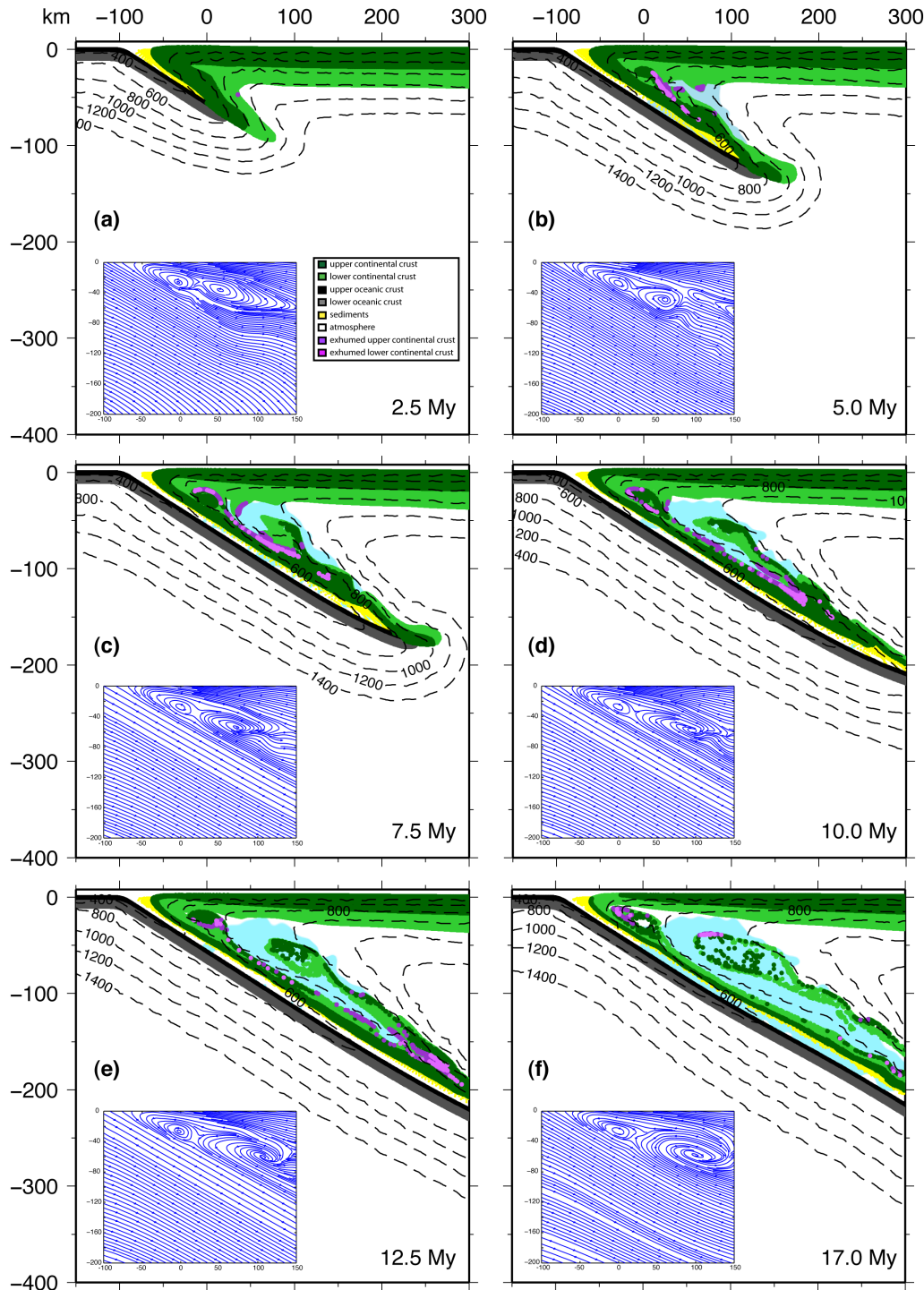


Figure 2. Evolution of run 015 (see Table 2) in six different stages (2.5 (a), 5 (b), 7.5 (c), 10 (d), 12.5 (e) and 17.0 (f) Ma). The legend illustrates the marker provenance. In the insets, streamlines (blue lines) obtained for the corner flow are reported.

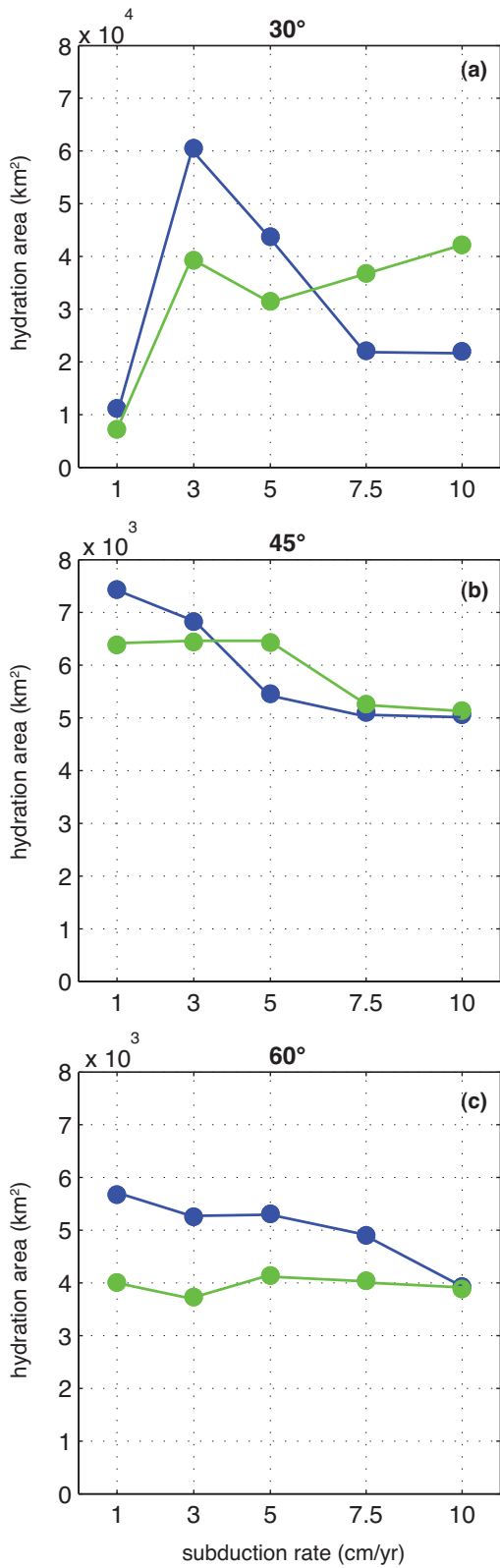


Figure 3. Hydration area vs. subduction rate for each slab dip: the blue points refer to dry dunite models and green points to dry olivine models.

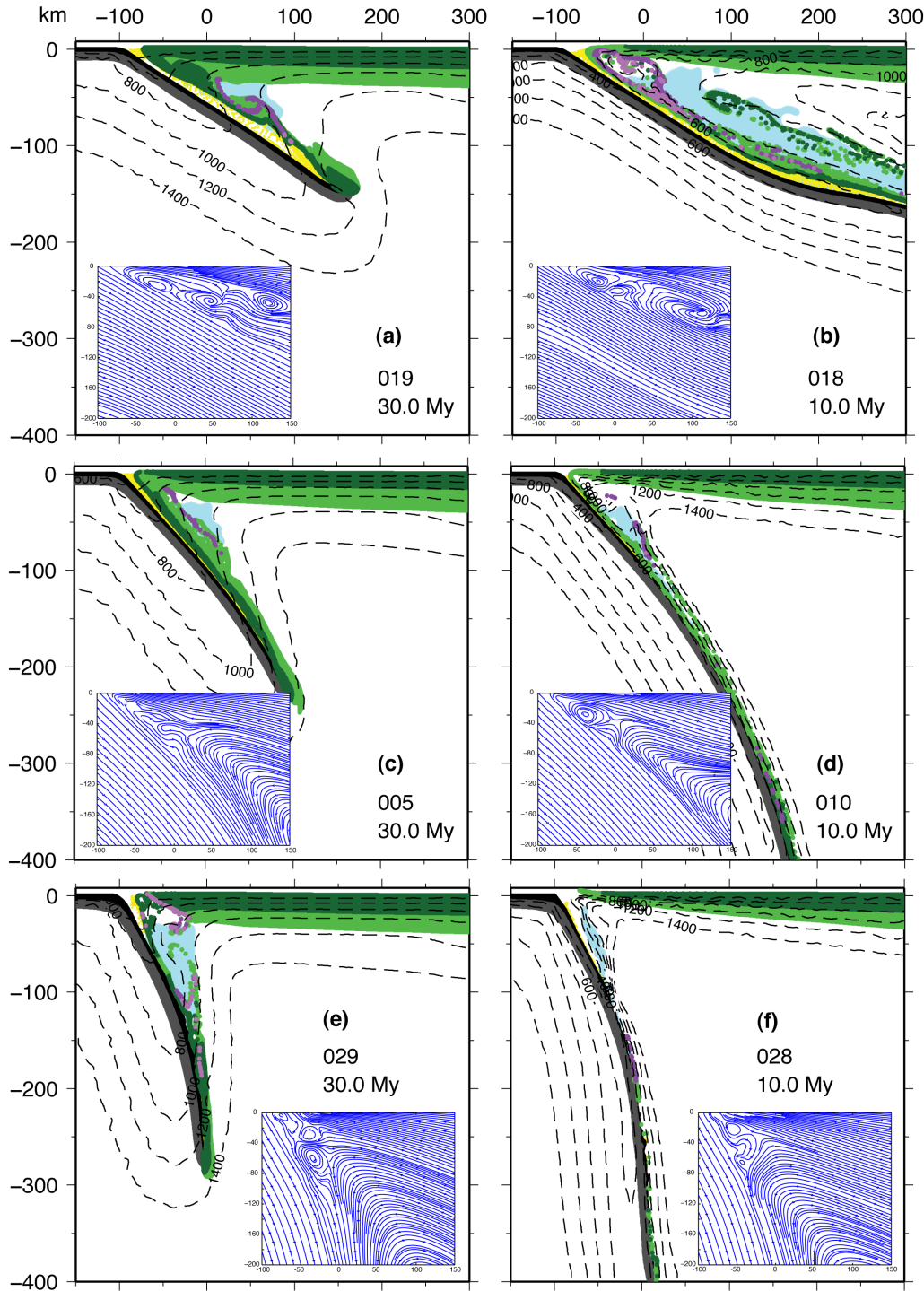


Figure 4. Final stage for runs 019, 018 (slab dip 30° , a, b), 005, 010 (slab dip 45° , c, d) and 029, 028 (slab dip 60° , e, f). Legend as in Figure 2. In the insets, streamlines (blue lines) obtained for the corner flow are reported.

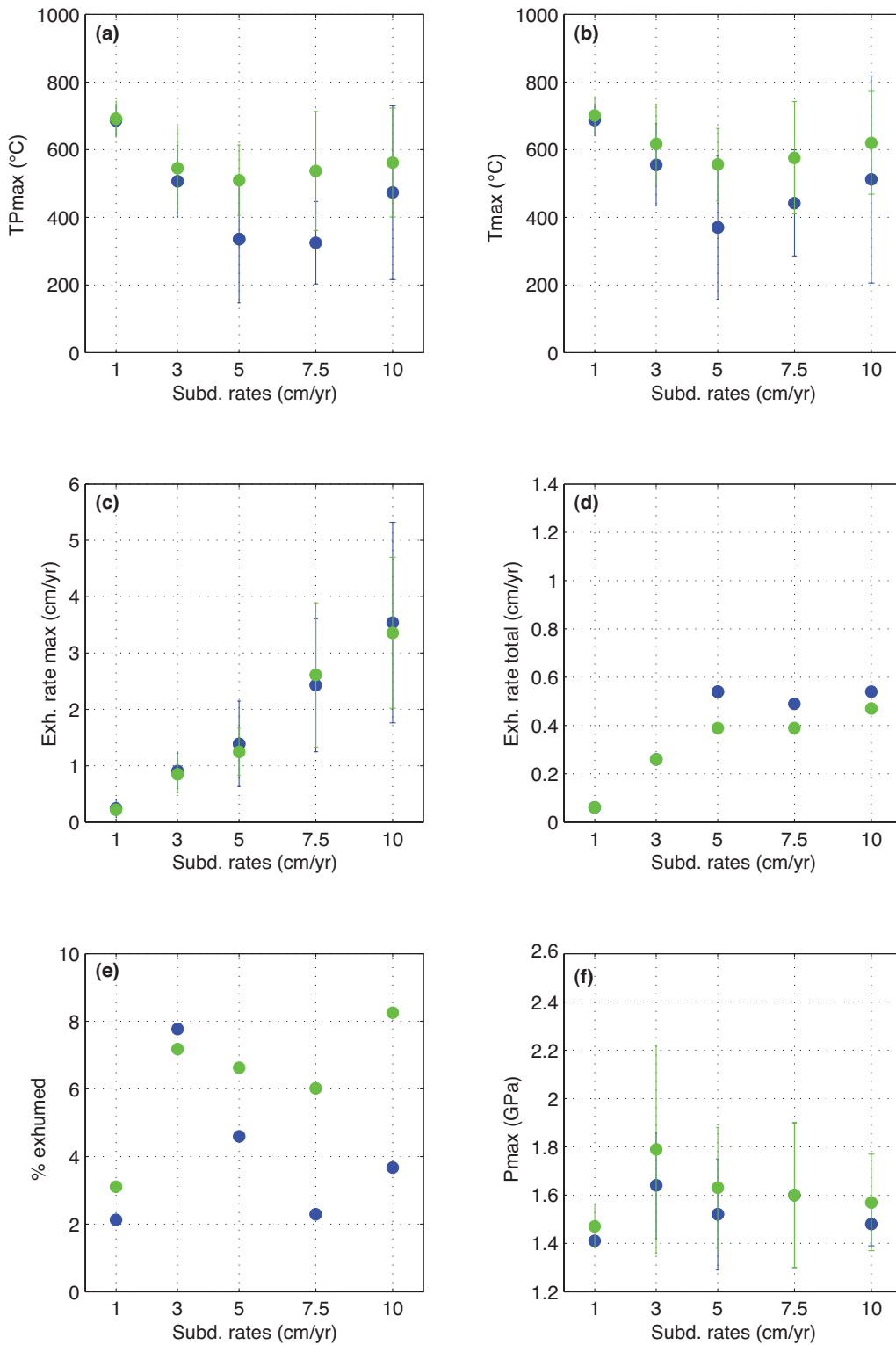


Figure 5. Statistical analysis of the exhumed crustal particles for 30° simulations: blue points refer to dry dunite models and green points to dry olivine models; vertical lines are the error-bars defined as standard deviation of mean values.

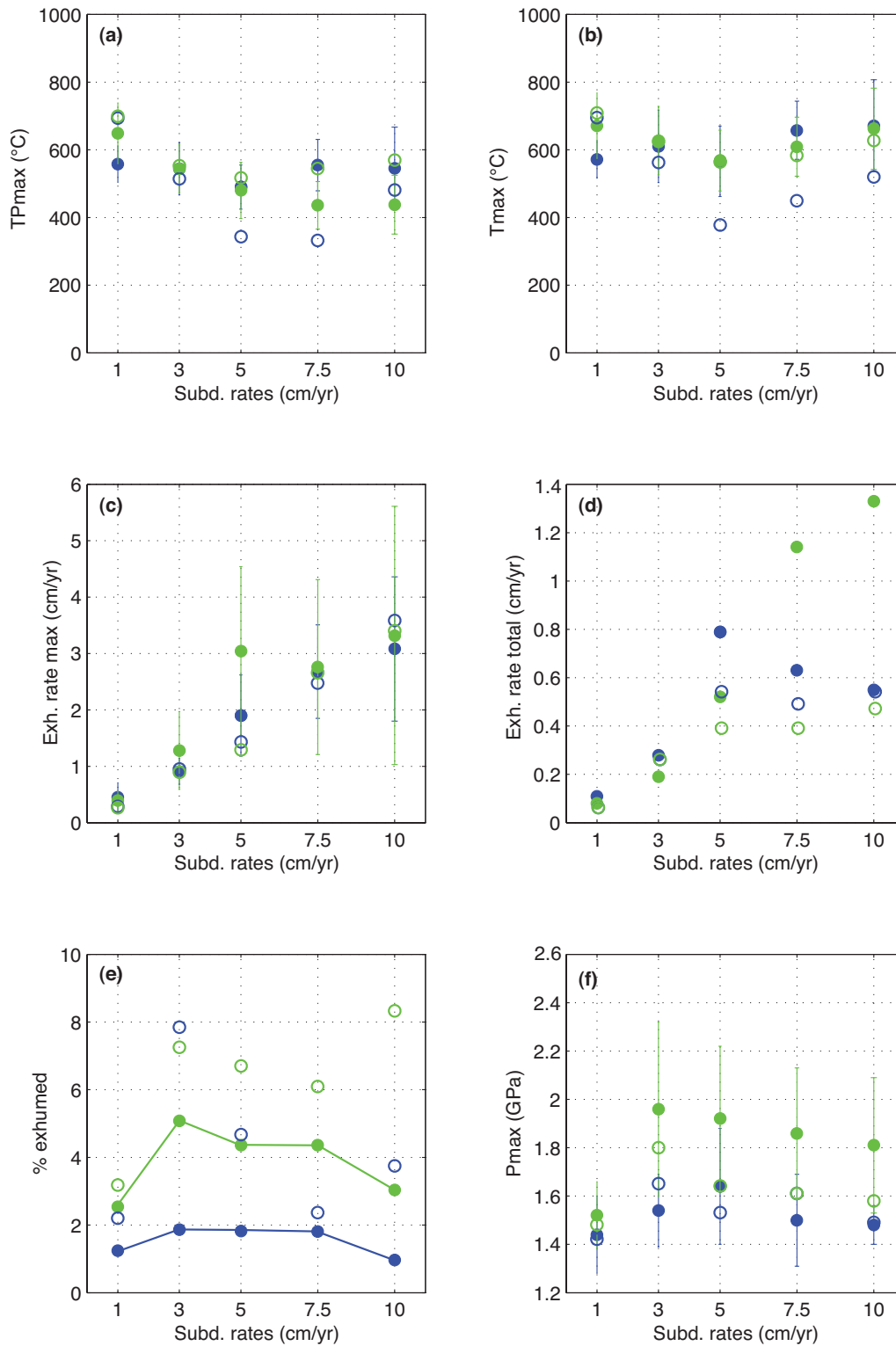


Figure 6. Statistical analysis of exhumed crustal particles for 45° simulations: blue points refer to dry dunite models and green points to dry olivine models; vertical lines are the error-bars defined as standard deviation of mean values. Empty circles are referred to 30° simulation data.

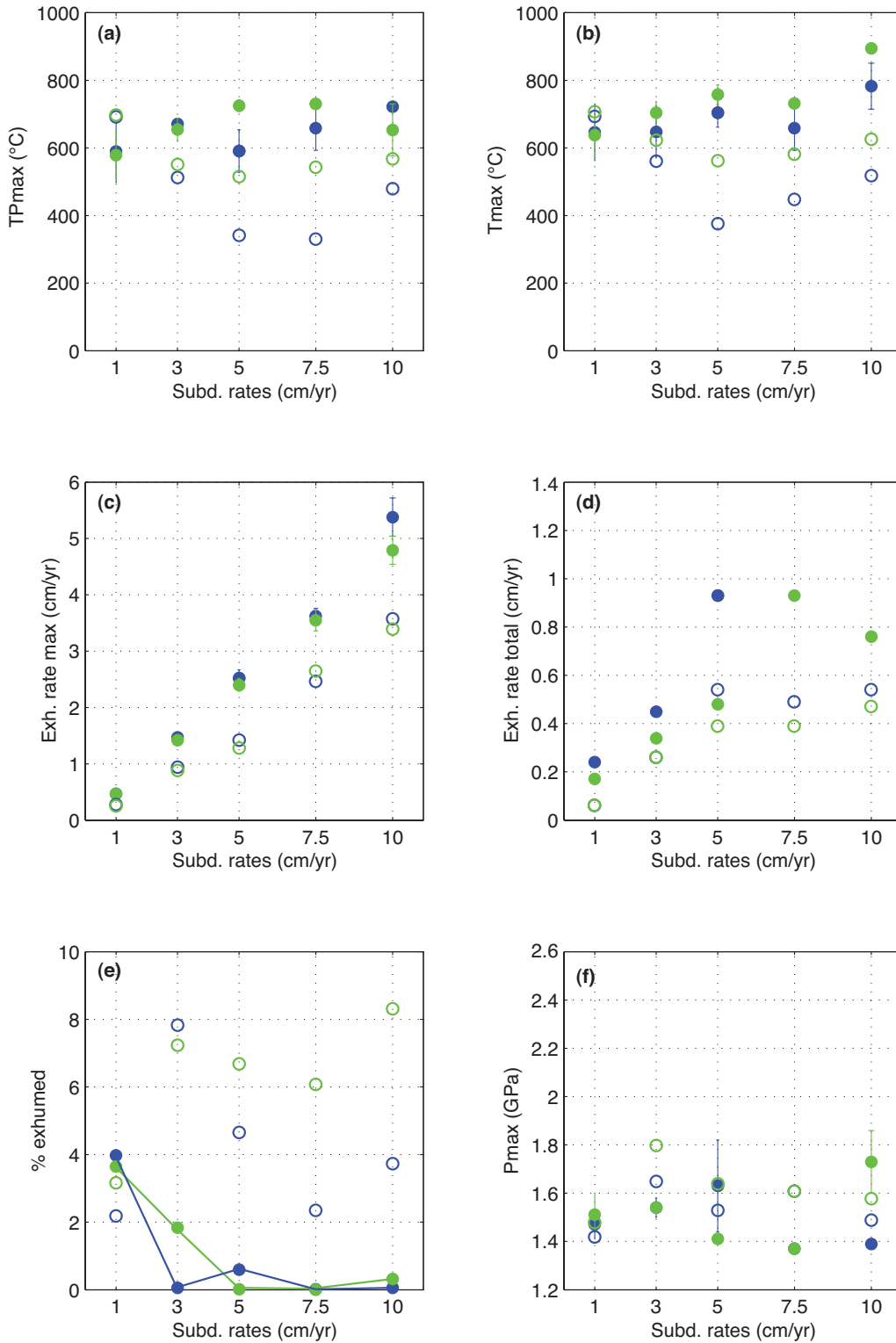


Figure 7. Statistical analysis of exhumed crustal particles for 60° simulations: blue points refer to dry dunite models and green points to dry olivine models; vertical lines are the error-bars defined as standard deviation of mean values. Empty circles are referred to 30° simulation data.

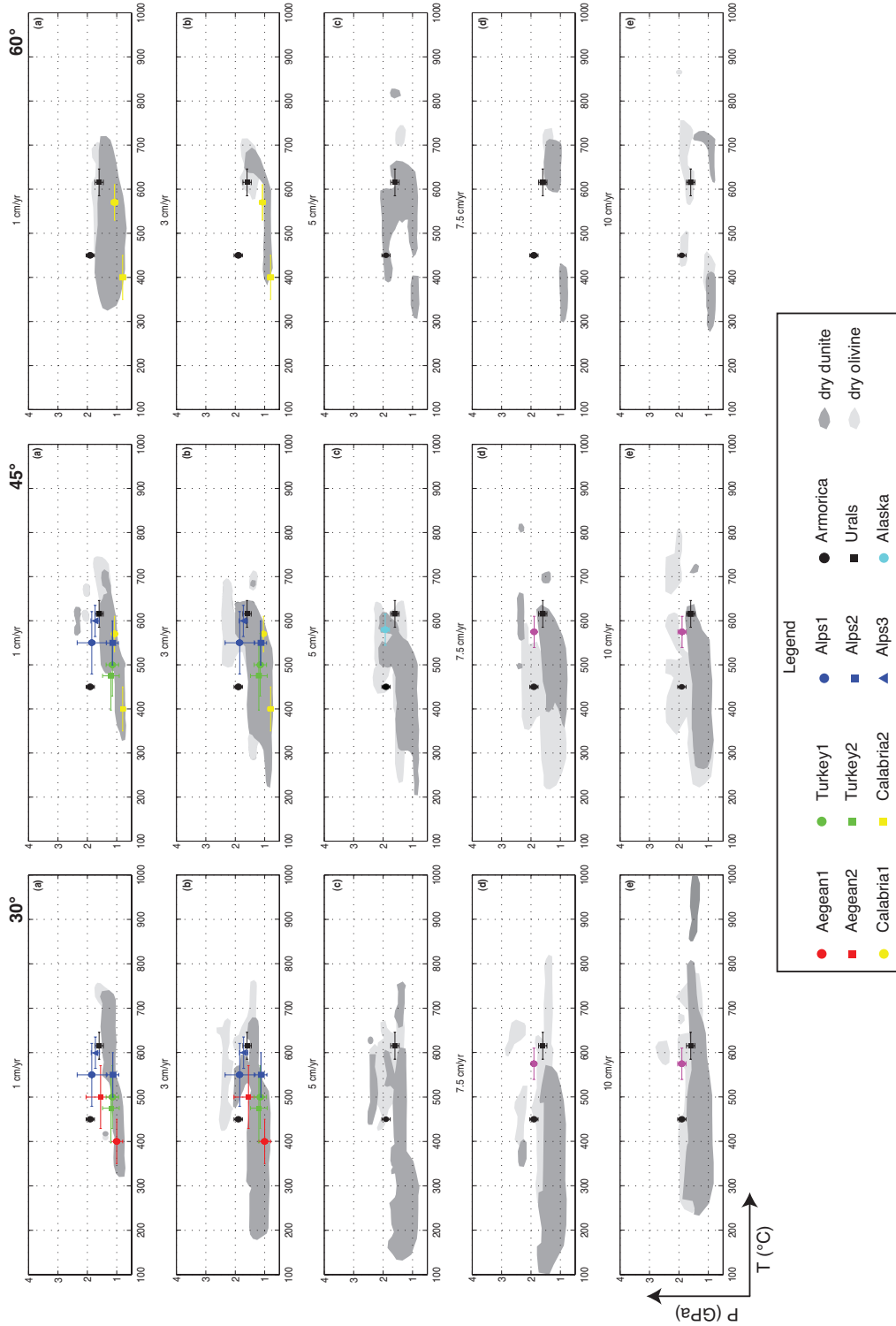


Figure 8. Comparison of simulated vs. natural PT estimates: colored symbols refer to units listed in Table 3. Vertical lines are the error-bars according to the original estimates.

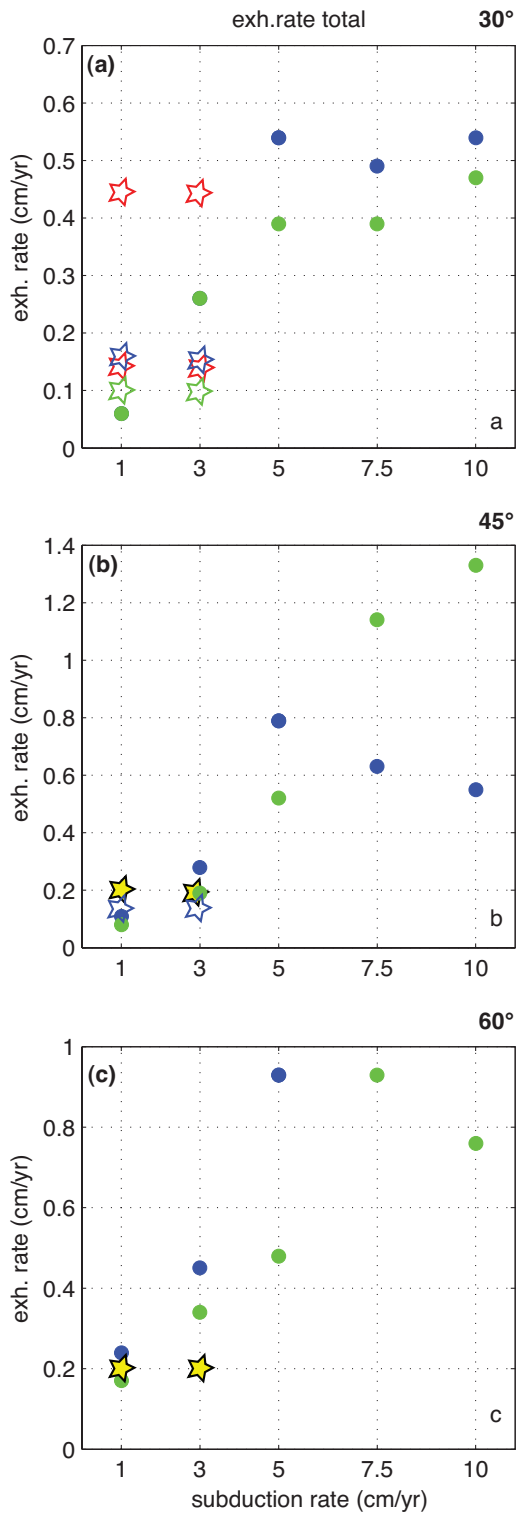


Figure 9. Simulated vs. natural exhumation rates: natural samples are represented by the stars. See the legend of Figure 8 for references. Blue points refer to dry dunite simulations and green points to dry olivine simulations.

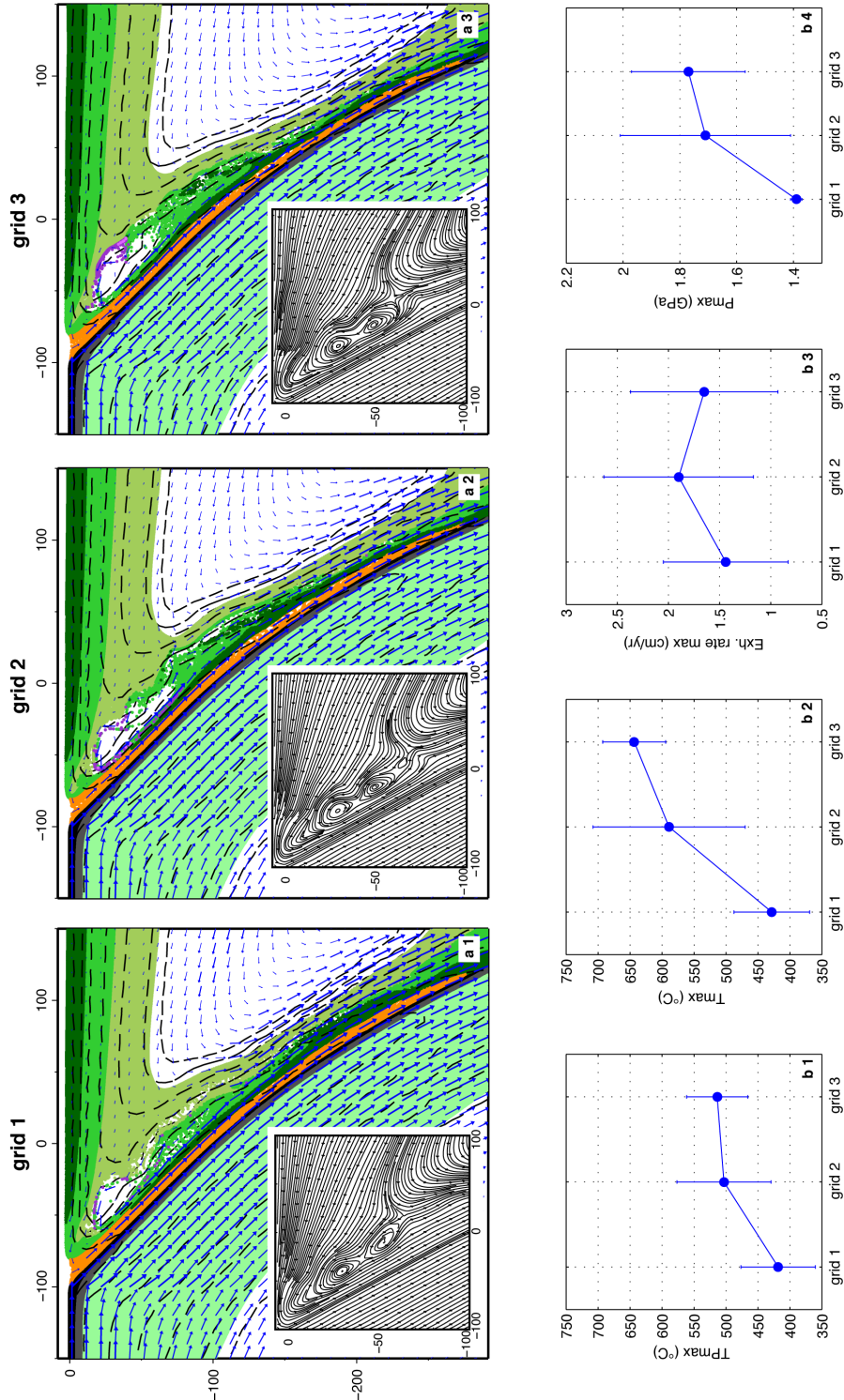


Figure 10. Results of the resolution test: in panels *a*_{*i*} the thermodynamic settings for 3 different grids (*a*₁, *a*₂, *a*₃) and the stream lines are displayed; legend as in Figure 2, lithospheric mantle markers are also shown. In panels *b*_{*i*} the statistical parameters, obtained for each grid, are displayed: *T*_{*P*max}, panel *b*₁; *T*_{max}, panel *b*₂; max. exh. rate, panel *b*₃; *P*_{max}, panel *b*₄.

Table 2. List of the performed numerical simulations.

Model ID	Slab velocity (cm/y)	Slab dip	Dry mantle viscosity law
019	1	30°	dry dunite
016	3	30°	dry dunite
015	5	30°	dry dunite
017	7.5	30°	dry dunite
018	10	30°	dry dunite
024a	1	30°	dry olivine
021a	3	30°	dry olivine
020a	5	30°	dry olivine
022a	7.5	30°	dry olivine
023a	10	30°	dry olivine
005	1	45°	dry dunite
008	3	45°	dry dunite
006	5	45°	dry dunite
009	7.5	45°	dry dunite
010	10	45°	dry dunite
014	1	45°	dry olivine
013	3	45°	dry olivine
007	5	45°	dry olivine
011	7.5	45°	dry olivine
012	10	45°	dry olivine
029	1	60°	dry dunite
026	3	60°	dry dunite
025a	5	60°	dry dunite
027	7.5	60°	dry dunite
028	10	60°	dry dunite
034	1	60°	dry olivine
031	3	60°	dry olivine
030	5	60°	dry olivine
032a	7.5	60°	dry olivine
033	10	60°	dry olivine

Table 3. Natural cases. References: (1) [Leech and Ernst, 2000], (2) [Ballevre et al., 2003], (3) [Brun and Faccenna, 2008], (4) [Rossetti et al., 2004], (5) [Thomson et al., 1998], (6) [Ring and Layer, 2003], (7) [Gosso et al., 2010], (8) [Gazzola et al., 2000], (9) [Thoni and Miller, 1996], (10) [Patrick, 1995], (11) [Whitney et al., 2008], (12) [Agard et al., 2009], (13) [Rondenay et al., 2008], (14) [Doglioni et al., 2007], (15) [Zucali et al., 2002].

Location	Unit Geology	P_{max} (GPa)	T_{max} ($^{\circ}C$)	Refs.	Sub.rate (cm/y)	Refs.	Slab dip	Refs.	Ex. rate (cm/y)	Refs.
Urals	Unit1	1.5-1.7	594-637	(1)					0.07-0.08	(1)
Armorica	eclog. micasc. Ile de Groix	1.8-2.0	450	(2)						
Calabr.1	micaschists Phyllite and orthoigneiss	1.2	<400	(3)	1-3	(3)	45-60	(14)	0.17-0.23	(3)
Calabr.2	Cont. sediments and marble	0.8 ± 0.1	400 ± 50	(4)	1-3	(3)	45-60	(14)	0.17-0.23	(3)
Aegean1	Continental phyllite-quartzite	1.0 ± 0.2	400 ± 50	(5)	1-3	(5)	30	(6)	0.4-0.5	(3)
Aegean2	Cyclades Blueschists	1.2-1.9	450-550	(6)	1-3	(5)	30	(6)	0.1-0.16	(6)
Alps1	Western Alps Lower Aosta Valley	1.5-2.2	500-600	(7)	1-3	(12)	30-45	(14)	0.14-0.18	(15)
Alps2	Central Alps, Languard-Campo	0.9-1.3	500-600	(8)	1-3	(12)	30-45	(14)		
Alps3	Koralpe-Saualpe Permian Gabbro	1.7-1.9	580-630	(9)	1-3	(12)	30-45	(14)		
Alaska	Brooks Range Orthogneiss	0.9-1.2	325-415	(10)	5	(13)	45	(13)		
Turkey1	Menderes Massive metasediment	1.0-1.3	450-550	(11)	1-3	(3)	30	(6)	0.08-0.11	(11)
Turkey2	Menderes Massive metasediment	1.0-1.4	420-530	(11)	1-3	(3)	30	(6)	0.08-0.11	(11)